Supplementary Information on:

Mass Spectrometry of Refractory Black Carbon Particles From Six Different Sources: Carbon Clusters and Oxygenated Ions

J. C. Corbin[1], B. Sierau[1], M. Gysel[2], M. Laborde[2,*], A. Keller[3], J. Kim[4], A. Petzold[4,**], T. B. Onasch[5,6], U. Lohmann[1] and A. A. Mensah[1]

[1]ETH Zurich, Institute for Atmospheric and Climate Science, Switzerland;

[2]Laboratory of Atmospheric Chemistry, Paul Scherrer Institute, 5232 Villigen PSI, Switzerland;

[3]Institute of Aerosol and Sensor Technology, University of Applied Sciences Northwestern Switzerland, Windisch, Switzerland;

[4]Deutsches Zentrum für Luft- und Raumfahrt, Institut für Physik der Atmosphäre, 82234 Oberpfaffenhofen, Germany.

[5]Aerodyne Research Inc., Billerica, Massachusetts, USA.

[6]Boston College, Chestnut Hill, Massachusetts, USA.

**Now at: Aerosol Consulting ML GmbH, Ennetbaden, Switzerland, & Ecotech Pty Ltd., Australia.*

***Now at: Institut für Energie- und Klimaforschung IEK-8: Troposphäre, Forschungszentrum Jülich GmbH, 52425 Jülich, Germany.*

1 SP-AMS Nomenclature

This section illustrates the distinctions between SP-AMS- and AMS-measured species in terms of a two-dimensional space: (i) vapourization temperature and (ii) light-absorption efficiency at 1064 nm. The purpose is to clarify the meaning of rCO_x in an SP-AMS context.

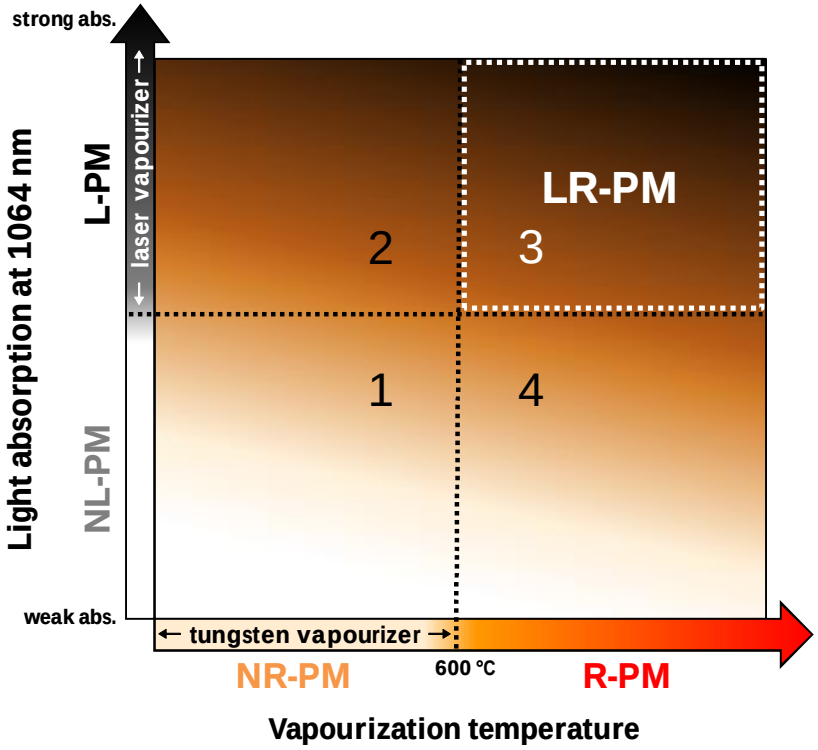

Figure S1. Illustration of the measurement domains of the AMS and SP-AMS vapourizers. The AMS vapourizes species which vapourize rapidly at 600 °C ("NR-PM"). The SP-AMS vapourizes species which absorb sufficient 1064 nm laser light ("L-PM"). The SP-AMS therefore provides the new measurement domain of refractory, 1064 nm light-absorbing PM ("LR-PM", smaller shaded region). The numbered regions are discussed in the text.

Figure S1 illustrates the distinction between PM species detectable by AMS ("NR-PM") and PM species detectable by SP-AMS but not AMS ("LR-PM"), as described in the main paper (Section 1). The horizontal axis, vapourization temperature, is the property upon which vapourization by the tungsten vapourizer of the AMS depends. The vertical axis, light-absorption at 1064 nm, is the property upon which vapourization by the laser vapourizer of the SP-AMS depends.

The AMS detects PM species which flash-vapourize upon impaction onto a 600 °C porous-tungsten vapourizer. Therefore, the AMS detects PM species in Regions 1 and 2, together termed "NR-PM" (non-

refractory particulate matter). PM species found in Region 1 include organic matter (OM), sulphates, nitrates, and ammonium. We do not know of any PM species found in Region 2.

The SP-AMS detects PM species which absorb sufficient light at 1064 nm to be vapourized by radiative heating. Therefore, the SP-AMS detects PM species in Regions 2 and 3. Region 3 is of special interest as it includes refractory black carbon particles (rBC), metallic particles, and absorbing minerals such as hematite. These refractory, 1064 nm light-absorbing particles are termed “LR-PM.” The present study focusses on rBC, which is a carbonaceous example of LR-PM.

Those PM species in Region 4 are not directly vaporized by AMS nor SP-AMS. Region 4 may include some types of organic matter, inorganic salts, or minerals such as kaolinite. Region 4 (and Region 1) species may be detected by the SP-AMS if they are internally-mixed with LR-PM of a higher vapourization temperature.

2 Selected Mass Spectra

This supplementary section includes the raw high-resolution mass spectra for two samples, in support of the discussion in the paper.

2.1 CBW

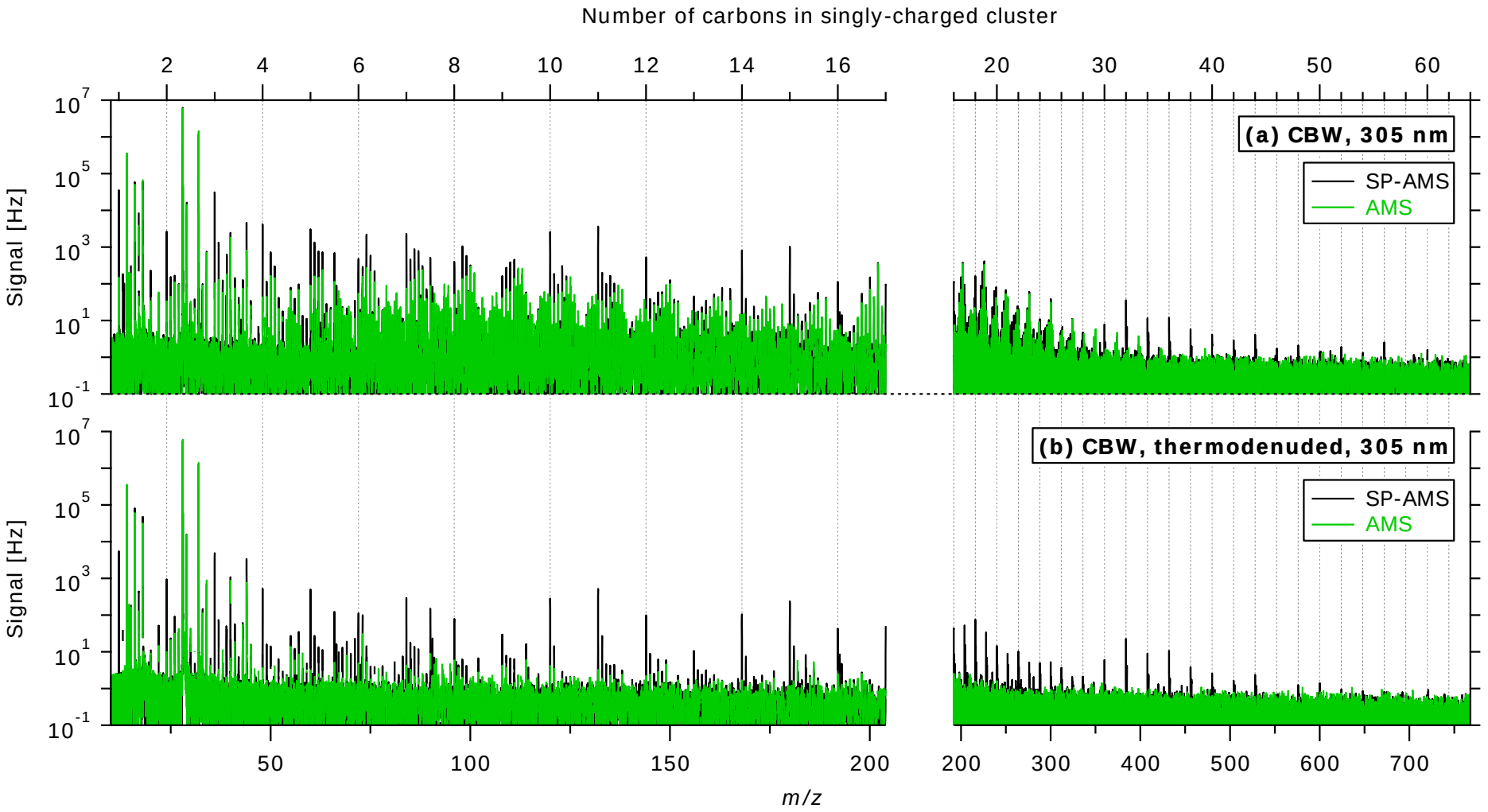

Figure S2. Mass spectra of (a) nascent CBW and (b) CBW thermodenuded at 250 °C. The left and right abscissas have different scales for clarity. All gridlines are spaced by 24 u (two carbon atoms). Background levels are about 0.5 Hz s^{-1} up to m/z 200 and decreasing at higher m/z in (a). The background is slightly lower in (b) since the reduced signals allowed the detector to relax between ion arrival events. After thermodenuding (b), the green AMS signals are considerably reduced, whereas C_x^{n+} signals (e.g. the fullerenes at m/z > 384) remain. The labelled diameter in (b) is the mobility size after thermodenuding.

2.2 FS

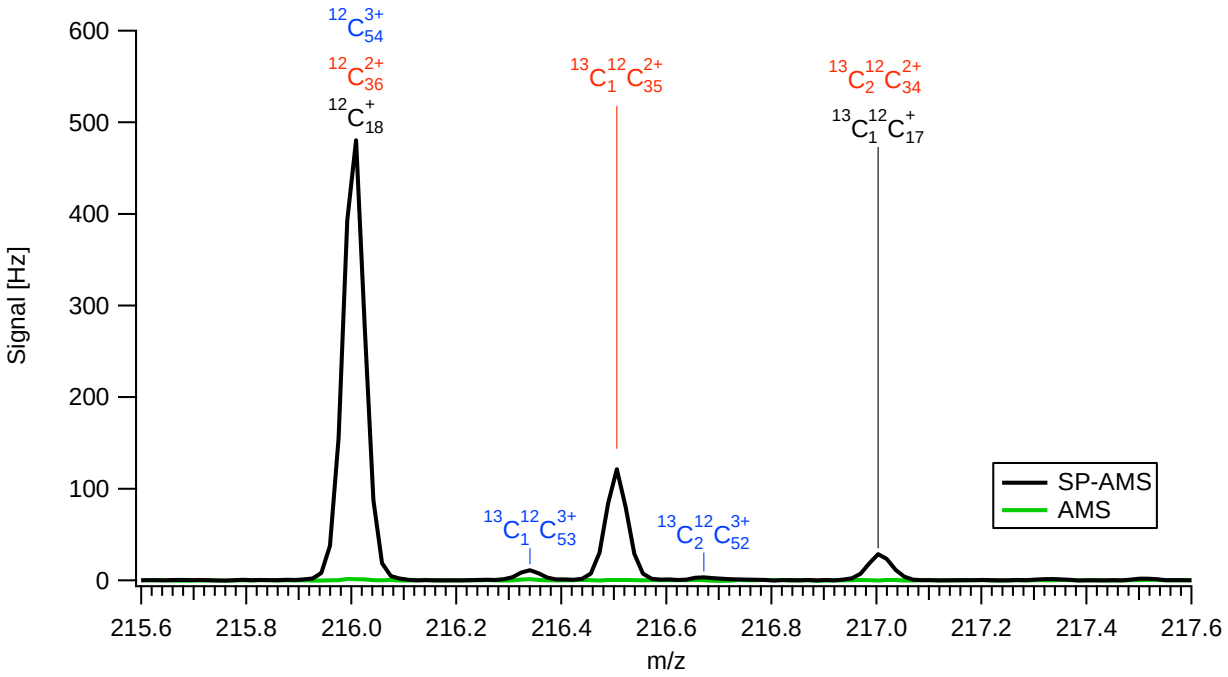

Figure S3. The three overlapping C_x^{n+} ions at m/z 216.00 (C_{18}^{+}, C_{36}^{2+}, and C_{54}^{3+}), indicated by the isotopic peaks as labelled. No C_{72}^{4+} isotope peak was observed (m/z 216.25). Gaussian fits to the peaks at m/z 216.33 and 216.66 match the predicted C_{54} isotopic ratio within uncertainty, whereas this ratio for m/z 216.00 to 216.50 is 24.7 ± 0.3 %, lower than the predicted 39.4 % for C_{36}. This indicates the presence of significant C_{18} at m/z 216.00 (and 217.00). Based on the isotopic peak areas at 216.33 and 216.50, the major peak at m/z 216.00 is 33.1 ± 0.6 % C_{18}, 62.8 ± 0.8 % C_{36} and 4.1 ± 0.6 % C_{54} using a relative abundance of carbon-13 of 1.08157 % (de Laeter et al., 2003). This abundance was confirmed at $^{13}C_1^{+}$.

3 SP-AMS C_x^+ Mass Spectra up to m/z 200

This section contains graphs for each rBC sample, corresponding to the data plotted in Figure 4 of the paper. The C_x^+ ions were fitted using PIKA 1.10H according to the software fitting routines. Since multiply-charged C_x^{n+} were observed for selected m/z (72, 192, …), isotopic constraints were removed during C_x^+ fitting. "C_x^+" is defined as $\mathbf{C}^+_{1 \le x \le 16}$ and the corresponding isotope ions, as explained in Section 3.1 of the paper.

3.1 FS

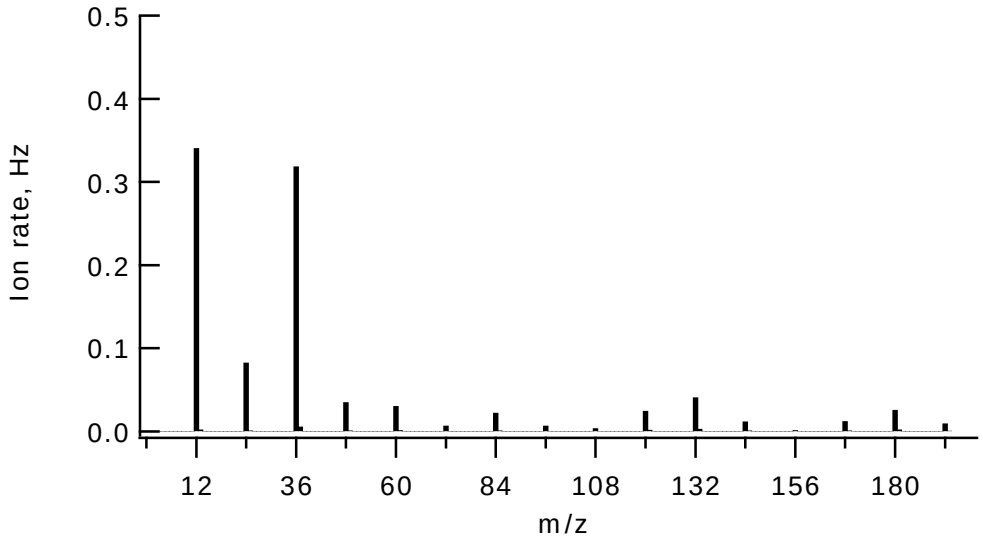

Figure S4. C_x^+ mass spectrum for Fullerene Soot (FS), showing nominally singly-charged ions $\mathbf{C}^+_{1 \le x \le 16}$.

3.2 CBW

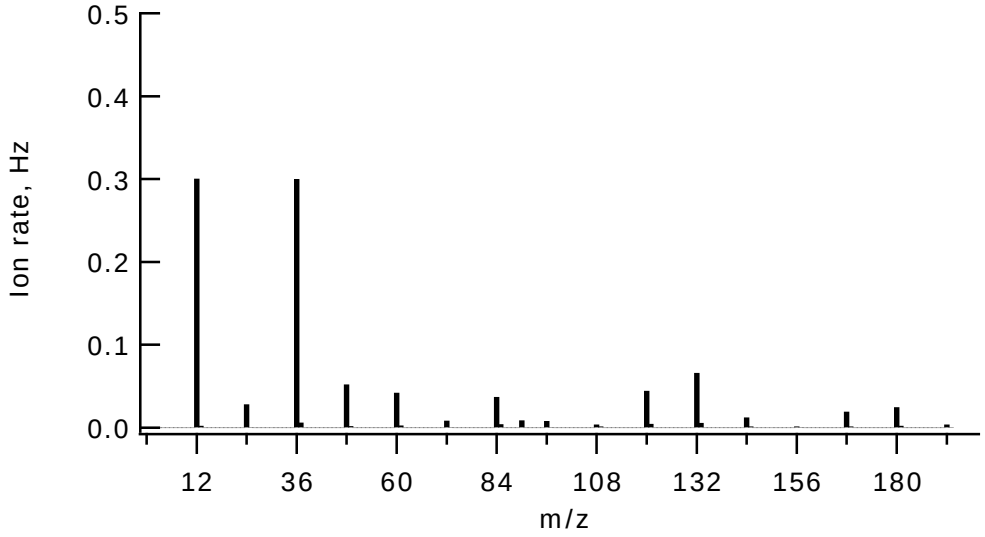

Figure S5. C_x^+ mass spectrum for CAST Brown, showing nominally singly-charged ions $C_{1 \le x \le 16}^+$.

3.3 GFG

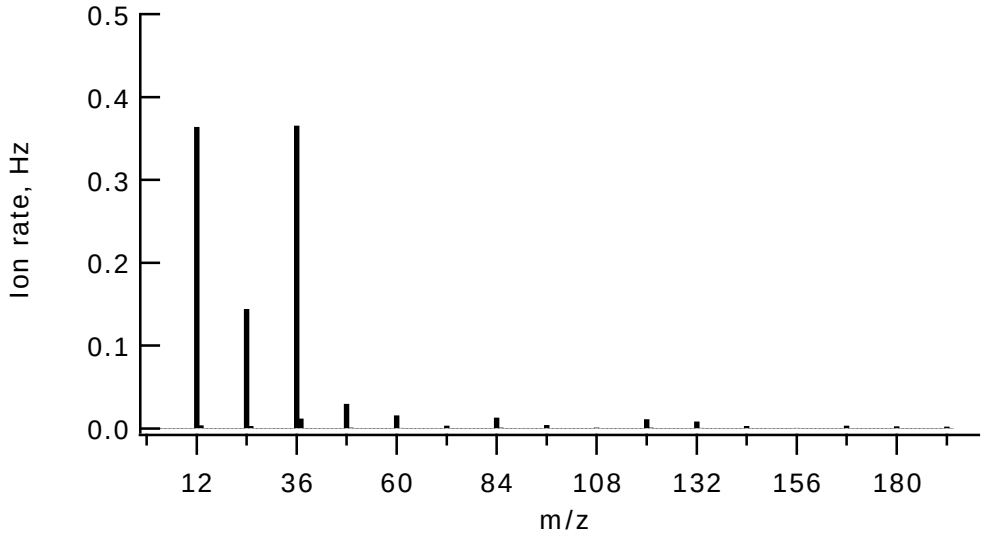

Figure S6. C_x^+ mass spectrum for GFG, showing nominally singly-charged ions $C_{1 \le x \le 16}^+$.

3.4 TU

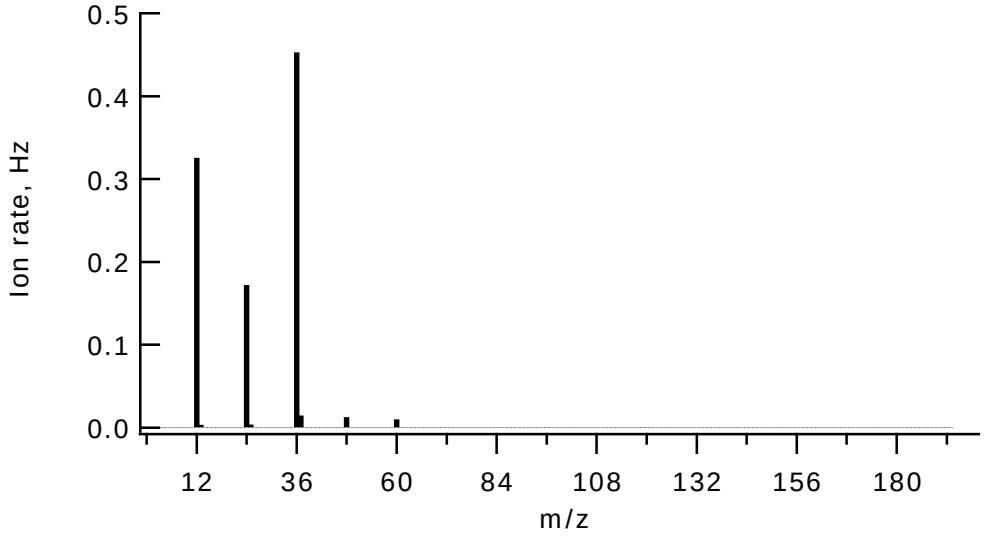

Figure S7. C_x^+ mass spectrum for aircraft-turbine particles, showing nominally singly-charged ions $C_{1 \le x \le 16}^+$.

3.5 RB

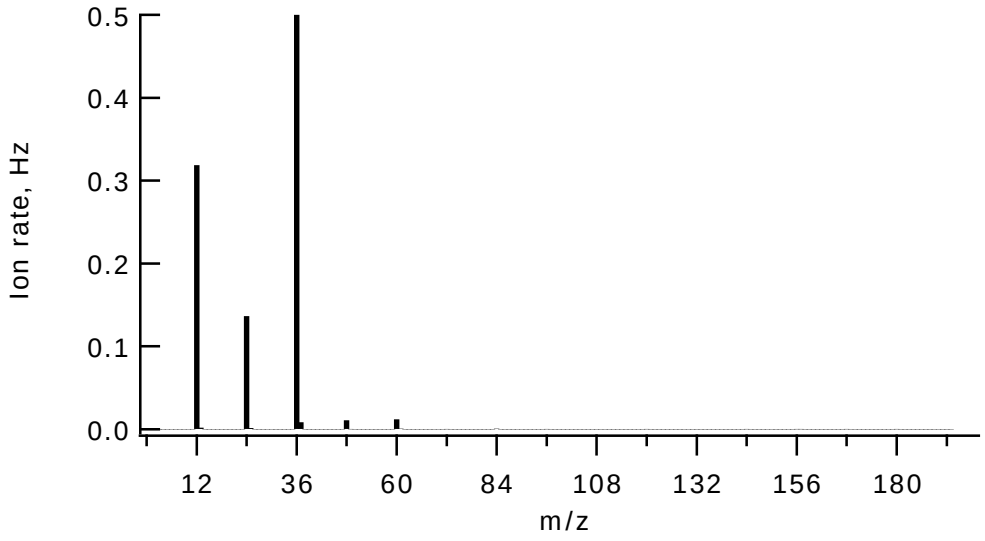

Figure S8. C_x^+ mass spectrum for Regal Black, showing nominally singly-charged ions $C_{1 \le x \le 16}^+$.

3.6 CBK

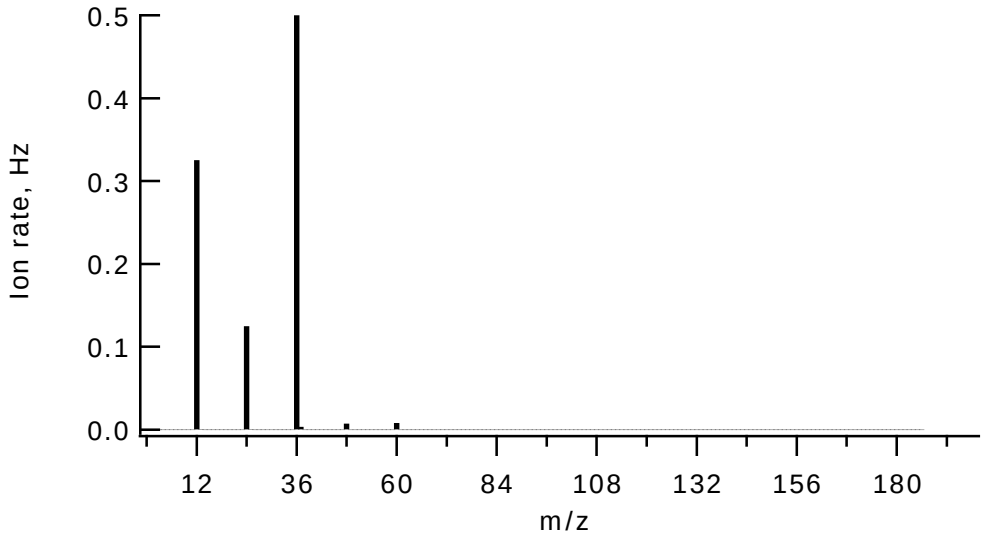

Figure S9. C_x^+ mass spectrum for CAST Black, showing nominally singly-charged ions $C_{1 \le x \le 16}^+$.

4 C_4^+ / C_3^+ signal ratio

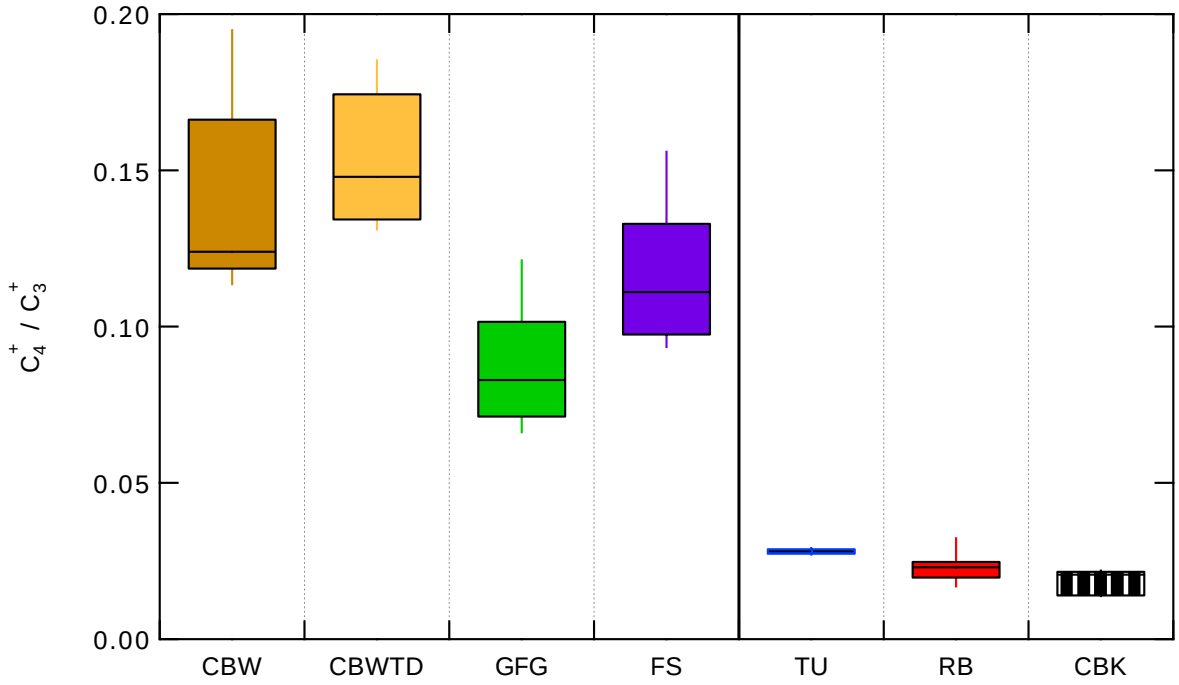

Figure S10. SP-AMS C_4^+ / C_3^+ ratios for CAST "Brown" (CBW), thermodenuded CBW (CBWTD), CAST "Black" (CBK), spark-generated particles (GFG), Fullerene-enriched Soot (FS), aircraft-turbine particles (TU), and Regal Black (RB). A similar distinction is seen as for C_1^+ / C_3^+ (Figure 4, main paper), in that the samples are divided according to their C_x^+ mass spectra. Some other ratios for $C_{x<6}^+$ also showed this trend, but all used $C_{x<3}^+$ and therefore would likely incur higher organic interferences than C_4^+ / C_3^+.

5 Refractory CO_2^+ in Particle Time-Of-Flight Mode

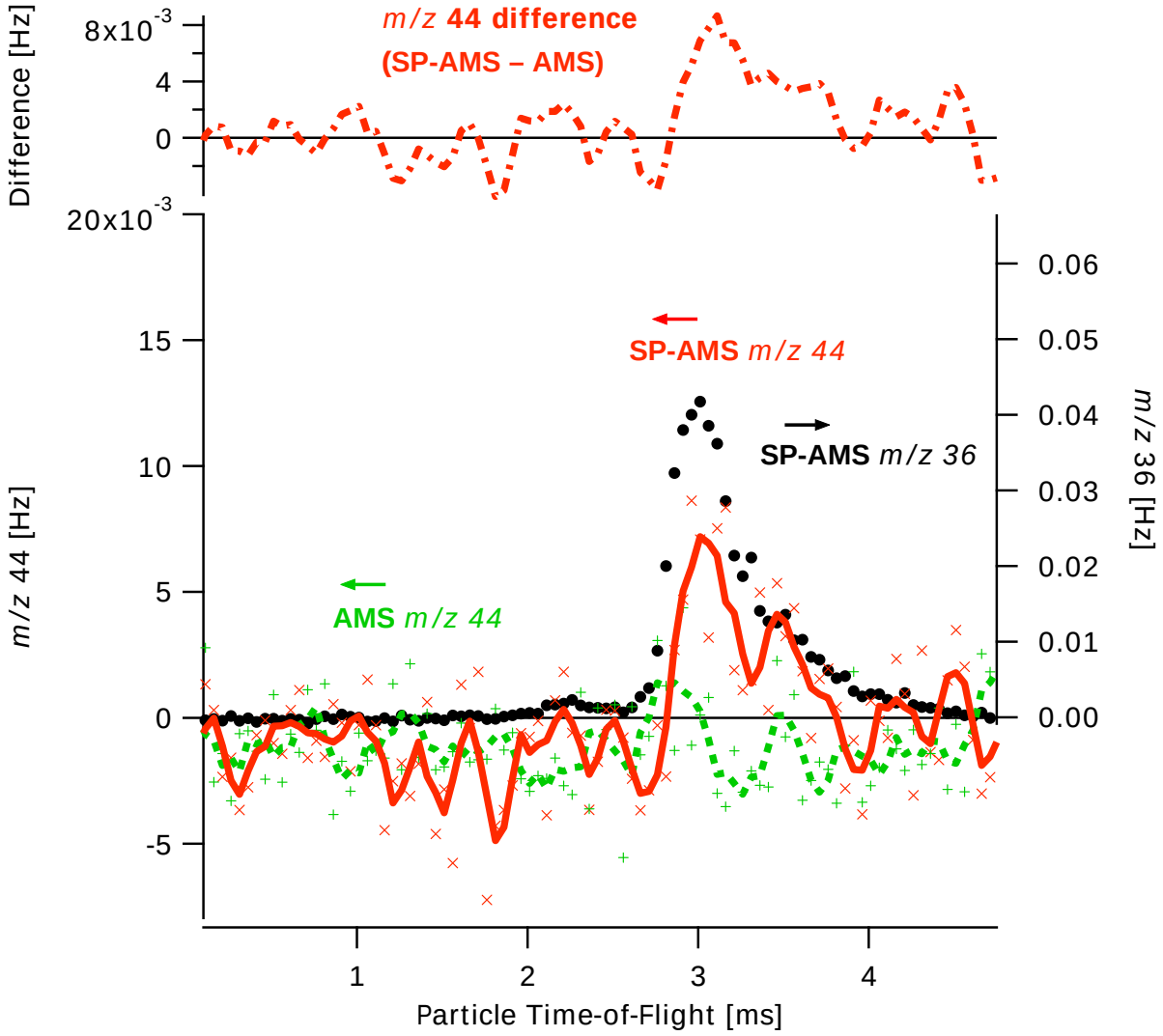

Figure S11. Signal at m/z 44 (CO_2^+) as a function of time for polydisperse Regal Black particles. SP-AMS raw data at m/z 44 are shown by × symbols, AMS data by + symbols. The • symbols show SP-AMS raw data at m/z 36. All m/z 44 data are plotted on the left axis whereas m/z 36 is plotted on the right. The lower curves (solid, SP-AMS; dashed, AMS) show the same data smoothed (4th-order 11-point Savitsky-Golay filter) and the upper curve is the difference of the two lower curves. The mode coincidences with that of m/z 28 in Figure 6 of the main text.

6 Additional Instrumentation

6.1.1 Single Particle Soot Photometer (SP2)

The Single Particle Soot Photometer (SP2, Droplet Measurement Technologies, Colorado USA) employs a 1064 nm continuous-wave Nd:YAG laser similar to that of the SP-AMS, but at a lower laser fluence (Onasch et al., 2012; Schwarz et al., 2010). Whereas the SP-AMS analyzes vapourized rBC, the SP2 measures the rBC incandescence resulting from laser heating. This incandescence can be calibrated to give the rBC mass per particle (Schwarz et al., 2006; Laborde et al., 2012). Complete details of SP2 operation and calibration during this study are provided by Gysel et al. (2012). The SP2 measured particles behind the same DMA as the SP-AMS.

6.1.2 Aerosol Particle Mass Analyzer (APM)

An Aerosol Particle Mass analyzer (APM, Kanomax APM-II, model 3601; (Ehara et al., 1996)) was used to determine the absolute mass of particles exiting the DMA. The APM introduces particles into the annular region between two rotating cylinders, across which a voltage is applied. The resulting centrifugal and electrostatic forces are then balanced to select particles of a given mass-to-charge ratio, independent of morphology. Particles of greater or lesser mass-per-charge are impacted on the cylinder walls.

The mass of singly-charged particles selected by the DMA was determined by scanning the APM voltage at fixed rotation speed. During a scan, the concentration of transmitted particles was monitored using a Condensation Particle Counter (CPC, TSI 3022, TSI Inc. USA). The single-particle mass was then determined from the mass setpoint at which the maximum number of particles was observed, as described in detail by Gysel et al. (2012).

7 Non-Refractory Particulate Matter

This section gives a general overview of the non-refractory particulate matter (NR-PM) of three of the six samples as a background to the C_x^{n+} spectrum discussion in the paper. The

remaining three samples (FS, RB and CBK) are not discussed in detail because they contained < 10 % NR-PM, based on a comparison of the AMS organic mass and the total mass estimated from the CPC number concentration and APM single-particle mass, using an SP2-based doubly-charged particle correction. A discussion of the NR-PM content of CBW, GFG and TU in the context of the main paper is given below.

7.1 CBW

For CBW, significant OM was observed by the AMS, with a mass spectrum indicative of polyaromatic hydrocarbons (PAHs) (Figure S2). This OM is consistent with thermal EC/OC analysis of a similar CAST burner (Schnaiter et al., 2006), and AMS measurements of soot from a different diffusion flame (Slowik et al., 2004). Compared to Slowik et al. (2004), the mass spectrum of our sample (Figure S2(a)) indicates a relatively greater contribution of hydrocarbon ions at m/z < 100, possibly due to a relatively high contribution from aliphatic compounds. In order to investigate the influence of these compounds on the SP-AMS mass spectrum, additional experiments were performed where CBW was thermodenuded at 250 °C prior to DMA selection. The resulting AMS mass spectrum (Figure S2(b)) showed almost negligible signal, while the SP-AMS spectrum retained the characteristic ions discussed in the paper.

7.2 GFG

Two sources of OM were possible for GFG particles, (i) contamination from the polyamide chamber of the generator (Roth et al., 2004) and contamination by OM from CBW, which was sampled immediately before GFG. CBW contamination was determined from the PAH fragmentation pattern at m/z 202 ($C_{16}H_{10}$), which was the major PAH signal. Signals from less-volatile PAH at higher m/z were not observed. A maximum organic mass of 16 % relative to the total APM-CPC mass was observed for the first GFG experiment after CBW (305 nm), which fell to < 8 % for the remaining experiments. No difference was observed in the C_x^{n+} spectrum over time for GFG, indicating that these contaminations did not influence the signals discussed in this paper.

186

187 It is worth noting that the SP2 was unable to bring GFG particles to incandescence, due to
188 exceptionally high conductive heat loss to the gas phase (Gysel et al., 2012). This is
189 discussed by Gysel et al. (2012) in terms of the fractal shape, very low effective density, and
190 very small primary-particle diameter (5 – 10 nm) of these particles. This cooling effect is
191 not expected to apply to the SP-AMS, since vapourization occurs in a near vacuum
192 (10^{-5} torr, (DeCarlo et al., 2006)), however, the fractal shape of GFG particles may result in
193 less efficient particle focussing by the AMS aerodynamic lens (Huffman et al., 2005).
194

195 7.3 TU

196 For airplane gas-turbine particles, the significantly different sampling configuration
197 required a different approach to the SP-AMS data. Turbine conditions were determined as
198 part of a larger initiative (Crayford, 2012), and monodisperse samples were not feasible.
199 The polydisperse particles were very small (mode diameter ~25 nm), irregularly-shaped,
200 and contained varying amounts of OM. Such small particles are poorly focussed by the AMS
201 aerodynamic lens, for which transmission begins to decrease dramatically below 60 nm for
202 spherical particles (Zhang et al., 2004). Focussing decreases further still for irregular
203 particles (Huffman et al., 2005), although this shape effect is weaker than the size effect.
204 Furthermore, particle focussing is more of an issue for the SP-AMS than the AMS, due to its
205 smaller vapourizer (SP-AMS laser full-width half-maximum: ~0.50 mm; AMS vapourizer:
206 3.81 mm diameter (Huffman et al., 2005; Onasch et al., 2012)), although the orthogonal
207 orientation of the SP-AMS laser beam to the particle beam may slightly increase its effective
208 area. A comparison of AMS and SP-AMS signals for TU is therefore non-trivial.
209

210 The at-times significant OM content of TU presents a separate problem. As organic
211 molecules generate C_x^+ ions for $1 < x < 3$ even in the AMS (albeit with much lower relative
212 yields than for rBC), interference in the SP-AMS spectrum by these ions can be expected. A
213 direct comparison of C_{1-3}^+ production between AMS and SP-AMS spectra is unjustified:
214 organic fragmentation during electron-impact mass spectrometry is affected by the initial
215 temperature of the molecule in question, as is well-known for the 600 °C AMS vapourizer

(Alfarra, 2004). For the SP-AMS, such differences in fragmentation have not been thoroughly characterized. Furthermore, with the SP-AMS laser on, an estimated 40 % of the AMS tungsten vapourizer may remain exposed to the incoming particle beam, assuming a particle beam the size of the vapourizer, a 3σ laser beam width, and a negligible parallax effect. This allows for a possible mixture of AMS and SP-AMS vapourization temperatures to exist in the vapourized particle plume. Such a mixture would complicate the mass spectrum, especially for poorly-focussed particles as expected for the turbine sample. Because the laser beam extends horizontally beyond the edges of the AMS vapourizer, this is an upper limit to the contribution of such AMS vapourization events.

In light of these two issues (organic production of C_{1-3}^+; vapourizer uncertainties for poorly-focussed particles), the current work only includes data where the AMS C_{1-3}^+ signal is minimal compared to the SP-AMS C_{1-3}^+ signal. Data from two sampling lines were available, one diluted by a factor of 10 and one undiluted. However, the above criterion resulted in the selection of engine emissions at maximum mass loading (2650 rpm) on the undiluted sampling line, where AMS C_1^+ and C_3^+ were 5 % and 1 % of the SP-AMS signals, respectively. It was initially expected that the diluted sampling line would have had reduced particulate organic loading and therefore less C_{1-3}^+ interference. However, this was not the case. Upon 10x dilution, the observed AMS signals at C_1^+ and C_3^+ decreased by a factor of ~10, whereas the SP-AMS signals decreased by a factor of ~30. This is consistent with a change in particle focussing due to changes in particle size and/or shape.

TU particle morphology on the diluted line was characterized by Tjong et al. (2012) during this experiment. Particles were aggregates of ~10 nm primary spherules. Larger particles appeared fractal under TEM. At a mobility diameter of 40 nm, particles exhibited mass-mobility exponents close to 2.75, reflecting the small number of primary spherules in the aggregate. These morphological features remained similar across the measured range of turbine thrusts, indicating that particles were comparable across these setpoints. Finally, the C_4^+/C_3^+ ratio was similar for all setpoints. The selected data (2650 rpm) are therefore considered representative for the discussion in the main paper.

8 Supplement References

Alfarra, M. R.: Insights Into Atmospheric Organic Aerosols Using An Aerosol Mass Spectrometer, PhD Thesis, Department of Chemical Engineering, University of Manchester, 2004.

Crayford, A., M. Johnson, R. Marsh, Y. Secvenco, D. Walters, P. Williams, A. Petzold, P. Bowen, J. Wang, D. Lister: SAMPLE III: Contribution to aircraft engine PM certification requirement and standard, Second Specific Contract, Final Report, European Aviatian Safety Agency, 2012.

de Laeter, J. R., Böhlke, J. K., De Bièvre, P., Hidaka, H., Peiser, H., Rosman, K., and Taylor, P.: Atomic weights of the elements. Review 2000 (IUPAC Technical Report), Pure and Applied Chemistry, 75, 683-800, 2003.

DeCarlo, P. F., Kimmel, J. R., Trimborn, A., Northway, M. J., Jayne, J. T., Aiken, A. C., Gonin, M., Fuhrer, K., Horvath, T., and Docherty, K. S.: Field-deployable, high-resolution, time-of-flight aerosol mass spectrometer, Anal. Chem., 78, 8281-8289, 2006.

Ehara, K., Hagwood, C., and Coakley, K. J.: Novel method to classify aerosol particles according to their mass-to-charge ratio—aerosol particle mass analyser, J. Aerosol Sci., 27, 217-234, 1996.

Gysel, M., Laborde, M., Mensah, A. A., Corbin, J. C., Keller, A., Kim, J., Petzold, A., and Sierau, B.: Technical Note: The single particle soot photometer fails to reliably detect PALAS soot nanoparticles, Atmos. Meas. Tech., 5, 10.5194/amt-5-3099-2012, 2012.

Huffman, J. A., Jayne, J. T., Drewnick, F., Aiken, A. C., Onasch, T. B., Worsnop, D. R., and Jimenez, J. L.: Design, modeling, optimization, and experimental tests of a particle beam width probe for the Aerodyne aerosol mass spectrometer, Aerosol Sci. Technol., 39, 1143-1163, 2005.

Laborde, M., Mertes, P., Zieger, P., Dommen, J., Baltensperger, U., and Gysel, M.: Sensitivity of the Single Particle Soot Photometer to different black carbon types, Atmos. Meas. Tech., 5, 10.5194/amt-5-1031-2012, 2012.

Onasch, T. B., Trimborn, A., Fortner, E. C., Jayne, J. T., Kok, G. L., Williams, L. R., Davidovits, P., and Worsnop, D. R.: Soot Particle Aerosol Mass Spectrometer: Development, Validation, and Initial Application, Aerosol Sci. Technol., 10.1080/02786826.2012.663948, 2012.

Roth, C., Ferron, G., Karg, E., Lentner, B., Schumann, G., Takenaka, S., and Heyder, J.: Generation of ultrafine particles by spark discharging, Aerosol Sci. Technol., 38, 228-235, 2004.

Schnaiter, M., Gimmler, M., Llamas, I., Linke, C., Jäger, C., and Mutschke, H.: Strong spectral dependence of light absorption by organic carbon particles formed by propane combustion, Atmos. Chem. Phys., 6, 2981-2990, 10.5194/acp-6-2981-2006, 2006.

Schwarz, J. P., Gao, R. S., Fahey, D. W., Thomson, D. S., Watts, L. A., Wilson, J. C., Reeves, J. M., Darbeheshti, M., Baumgardner, D. G., Kok, G. L., Chung, S. H., Schulz, M., Hendricks, J., Lauer, A., Kärcher, B., Slowik, J. G., Rosenlof, K. H., Thompson, T. L., Langford, A. O., Loewenstein, M., and Aikin, K. C.: Single-particle measurements of midlatitude black carbon and light-scattering aerosols from the boundary layer to the lower stratosphere, Journal of Geophysical Research, 111, 10.1029/2006JD007076, 2006.

Schwarz, J. P., Spackman, J. R., Gao, R. S., Perring, A. E., Cross, E., Onasch, T. B., Ahern, A., Wrobel, W., Davidovits, P., Olfert, J., Dubey, M. K., Mazzoleni, C., and Fahey, D. W.: The Detection Efficiency of the Single Particle Soot Photometer, Aerosol Sci. Technol., 44, 612-628, 10.1080/02786826.2010.481298, 2010.

Slowik, J. G., Stainken, K., Davidovits, P., Williams, L., Jayne, J., Kolb, C., Worsnop, D. R., Rudich, Y., DeCarlo, P. F., and Jimenez, J. L.: Particle morphology and density characterization by combined mobility and aerodynamic diameter measurements. Part 2: Application to combustion-generated soot aerosols as a function of fuel equivalence ratio, Aerosol Sci. Technol., 38, 1206-1222, 2004.

Tjong, H., Rogak, S., Olfert, J., Johnson, T., Symonds, J., Thomson, K., and Smallwood, G.: Morphology of particles produced by aviation gas turbines, 31st Annual American Association for Aerosol Research Conference, Minneapolis, 2012.

Zhang, X., Smith, K. A., Worsnop, D. R., Jimenez, J. L., Jayne, J. T., Kolb, C. E., Morris, J., and Davidovits, P.: Numerical characterization of particle beam collimation: Part II integrated aerodynamic-lens–nozzle system, Aerosol Sci. Technol., 38, 619-638, 2004.